Petroleum Science 20 (2023) 1742–1749

Contents lists available at ScienceDirect

Petroleum Science

journal homepage: www.keaipublishing.com/en/journals/petroleum-science

Original Paper

Thermal conductive proppant with self-suspension ability

Guo-Qing Xu [a, 1], Xiu-Ping Lan [b, 1], Si-Si Zhao [b], Kai-Yi Hu [b], Si-Meng Qi [b], Li-Dong Geng [a, *], Quan Xu [b, **], Yang Zhou [b, ***]

[a] Sinopec Key Laboratory of Drilling Completion and Fracturing of Shale Oil and Gas, SINOPEC Research Institute of Petroleum Engineering Co., Ltd, Beijing, 102249, China

[b] State Key Laboratory of Petroleum Resources and Prospecting, Beijing Key Laboratory of Biogas Upgrading Utilization, Harvard SEAS-CUPB Joint Laboratory on Petroleum Science, China University of Petroleum (Beijing), Beijing, 102249, China

ARTICLE INFO

Article history:
Received 5 July 2022
Received in revised form
23 November 2022
Accepted 23 November 2022
Available online 25 November 2022

Edited by Yan-Hua Sun

Keywords:
Exploitation of shale oil
In situ mining Technology
Thermally conductive proppant
Heat transfer

ABSTRACT

The *in situ* mining technology is applied to the exploitation of medium- and low-maturity shale oil, which can use heaters to warm up the oil shale formations and pyrolyze the kerogen. Due to the low thermal conductivity of oil shale, electric heaters need extra equipment to improve heat transfer efficiency. In this study, a thermally conductive proppant is fabricated by coating epoxy-resin and graphite on ceramic proppants for the first time, which could support the fracturing crack and transfer heat. The thermal conduction property of epoxy-resin and graphite coated proppants (EGPs) is 245% higher than that of uncoated proppants, which can transfer more heat to the oil shale formation and accelerate the conversion of kerogen. The adhesive property of EGPs is improved by 47.9% under the load force of 1500 nN, which prolongs the time for the fracture to close. In summary, this novel proppant is expected to assist in-situ mining technology in the production of medium and low-maturity shale oil.

1. Introduction

Oil shale is an ash-rich sedimentary rock that contains a lot of combustible organic matter (Xu et al., 2022; Zhang et al., 2019b, 2020). Most of the organic matter in oil shale is kerogen, which is insoluble in common organic solvents (Faisal et al., 2020; You et al., 2019; Zhang et al., 2021). Oil shale resources are abundant, with shale oil reserves reaching 689 billion tons, which is several times the recoverable reserves of crude oil in the world (You et al., 2018; Wang et al., 2020; Han et al., 2018). As oil supplies continue to decline and the cost of petroleum-based products rises, shale oil will have the opportunity to fill the world's fossil energy gap in the coming years (Hu et al., 2019; Wang Q. et al., 2018; Wang et al., 2019; Wang S. et al., 2021). Kerogen in oil shale is completely solid in its natural state and cannot be recovered as natural oil or gas in reservoirs (Taheri-Shakib and Kantzas, 2021; Raja et al., 2017; Lee et al., 2018). Kerogen in oil shale can only be converted into liquid shale oil and gas through pyrolysis (Gai et al., 2018; Han et al., 2019; Hu et al., 2022a). *In situ* mining technology is considered to be the most potent way to exploit oil shale resources (Wang H. et al., 2021; Zhang et al., 2019a; Zhao et al., 2018; Zhu et al., 2018). Electric heating technology is one of the most mature *in situ* mining technologies for oil shale (Hu et al., 2022b; Ju et al., 2021; Yang et al., 2019, 2021). In the electric heating technology, a fracture crack is generated by hydraulic fracturing, which is filled with a heat-conducting medium to transfer heat, where the shale formation is pyrolyzed to produce shale oil (Li H. et al., 2020; Meng et al., 2020; Pei et al., 2018; Wang L. et al., 2018). The proppant is an important material in hydraulic fracturing (Zoveidavianpoor and Gharibi, 2015; Xu et al., 2021; Zhao et al., 2020). The proppant with heat transfer can act as the heat-conducting medium in the fracture crack of the shale formation, which can transfer heat to oil shale as well as support the fracture crack (Fig. 1) (Ren et al., 2019; Luo et al., 2021; Li et al., 2022). At present, functional proppants include multiphase flow water-decreasing proppants, expandable proppants, traceable proppants, and proppants for enhanced gas recovery (Danso et al., 2021; Krishnan et al., 2021; Lan et al., 2020; Sun et al., 2022; Xiao et al., 2021). However, the process of transferring heat of these proppants is inefficient, which is difficult to be

* Corresponding author.
** Corresponding author.
*** Corresponding author.
E-mail addresses: gengld.sripe@sinopec.com (L.-D. Geng), xuquan@cup.edu.cn (Q. Xu), zhouyang@cup.edu.cn (Y. Zhou).
[1] Guo-Qing Xu and Xiu-Ping Lan contributed equally to this work.

https://doi.org/10.1016/j.petsci.2022.11.022

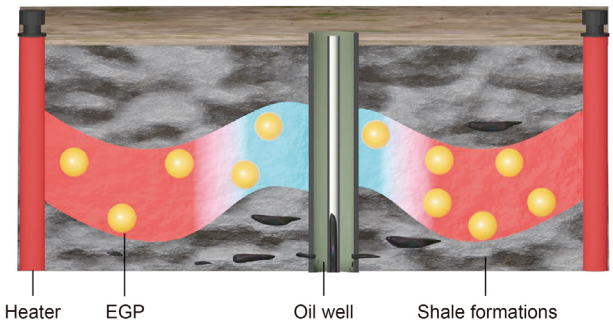

Fig. 1. Schematic diagram of EGP application *in situ* mining technology.

applied to in-situ mining technology (Gol et al., 2017; He et al., 2021; Kang et al., 2020). Therefore, it is urgent to design a thermally conductive proppant for the in-situ conversion of shale oil, so as to improve the conversion efficiency of shale oil (Bandara et al., 2021; Cao et al., 2020; Chen et al., 2021; Fu et al., 2016).

In this work, for the first time, we have prepared a thermally conductive proppant successfully. This novel proppant has better adhesive properties, which will make the EGPs easier to stay in the fracture crack. The temperature of EGPs is 245% higher than the uncoated proppant when the time point is 9 s. The excellent thermal conduction property of EGPs could provide more heat to the oil shale formation. Meanwhile, the ratio of floating of EGPs is increased by 77.5% in deionized water. This demonstrates that the EGPs will have a good distribution in the fracture crack. The liquid conductivity of EGPs is enhanced by 21.4% at a closure pressure of 5 MPa, which can improve oil and gas transportation efficiency.

2. Materials and methods

2.1. Materials

The epoxy-resin e-51 and curing agent T31 were obtained from Kunshan Jiulimei Electronic Materials Co., Ltd. The guar gum was provided by Xiya Reagent. The absolute ethanol was obtained from Tianjin Zhiyuan Chemical Reagent Co., Ltd. Graphite, graphene, and multi-walled carbon nanotubes were obtained from Shanghai McLean Biochemical Technology Co., Ltd. Copper powder, silver nanoparticles, and boron nitride were provided by Shanghai Aladdin Biochemical Technology Co., Ltd. Ceramic proppant was obtained from the market.

2.2. Preparation of heat transfer proppants

The epoxy-resin precursor was prepared in a fixed mass proportion (epoxy-resin: thermally conductive material = 7:3). Then the curing agent T31 was added to the epoxy-resin precursor in a fixed proportion (epoxy-resin e-51: curing agent T31 = 3:1). The ceramic proppants were added to the epoxy-resin precursor in a fixed proportion (epoxy-resin e-51: ceramic proppant = 1:3) and stirred for 5 min. The graphite was added to the mixture in a mass proportion (epoxy-resin: graphite = 7:3) and stirred for 5 min. The

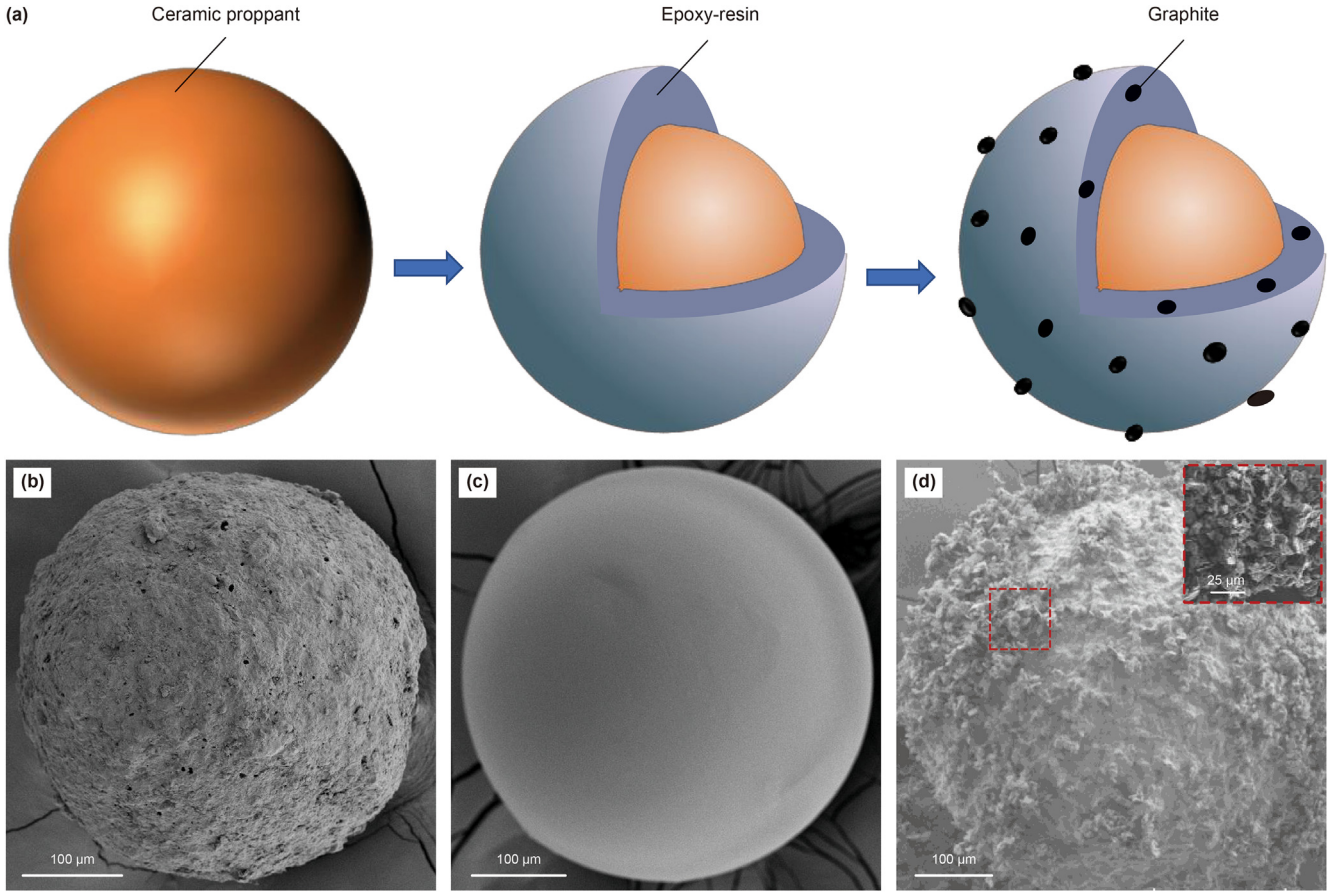

Fig. 2. (**a**) Structure diagram of the EGP. SEM micrographs of the ceramic proppant (**b**), epoxy-resin coated proppant (**c**), and EGP (**d**), respectively. The inset is the SEM micrograph of the graphite.

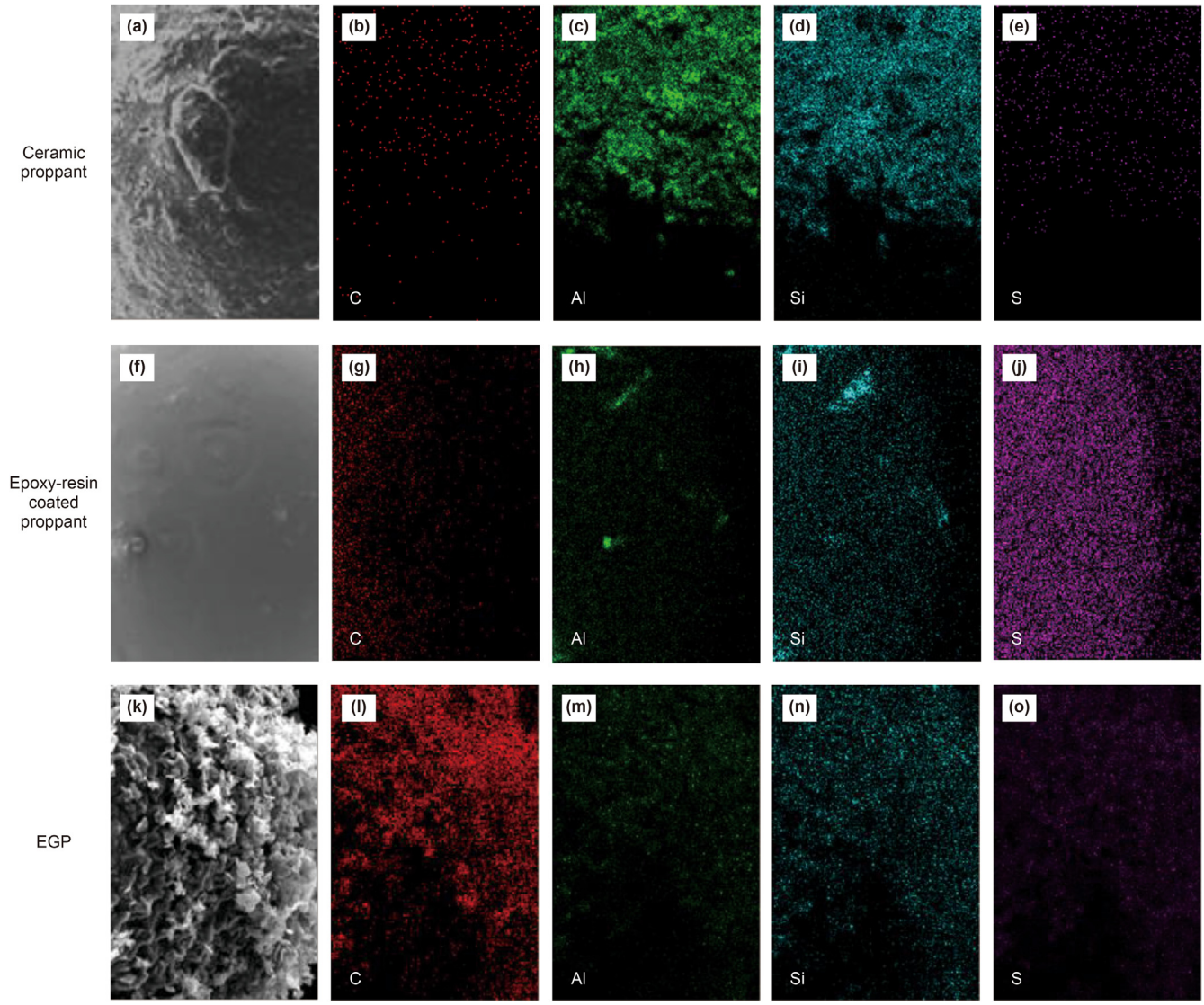

Fig. 3. SEM micrographs of ceramic proppant (**a**), epoxy-resin coated proppant (**f**), and EGP (**k**). Carbon (**b, g, l**), aluminum (**c, h, m**), silicon (**d, i, n**), and sulfur (**e, j, o**) elements on the surface of different proppants.

mixture was dried under indoor conditions for 24 h (25 °C, 101.325 kPa). The cool block-shaped proppant was ground by mortar to obtain several small block-shaped proppants. Finally, the small block-shaped proppants were ground into granule by the mortar and sample sieve.

2.3. Characterization

Samples were characterized by a scanning electron microscope (SEM, Zeiss sigma 500) and an energy dispersive X-ray analyzer (EDX, Bruker Xflash 6/30). The contact angle of the proppant was measured by an optical contact angle measuring instrument (SDC-200) with a test accuracy is 0.1°. The test temperature and test pressures were 27 °C and 101.325 kPa. Deionized water and the guar gum solution were liquid samples. The liquid conductivity of the proppants was tested by a liquid conductivity tester FCS-842. Deionized water was supplied as a fracturing liquid.

2.3.1. Fourier transform-infrared spectroscopy (FT-IR)

The FT-IR spectra of the proppants and graphite were measured by a Bruker VERTEX 70. The dried sample was mixed with ground KBr to prepare flakes. The measurements were carried out in the range of 4000–500 cm^{-1} wavenumber.

2.3.2. X-ray diffraction (XRD)

The XRD patterns of proppants and graphite were measured by a Bruker D2 PHASER, which could characterize the crystallinity of samples. The test range and test accuracy are 5°–90° and ±0.02°.

2.4. Adhesive experiment

The adhesive force of proppant test was accomplished using a Bruker Dimension Icon. The parameters of the probe are as follows. The thermal tune range is 5–2000 kHz. The power spectral density (PSD) bin width is 47.7 Hz. The deflection sensitivity is 54.88 nm/V. The spring constant is 172.5 N/m.

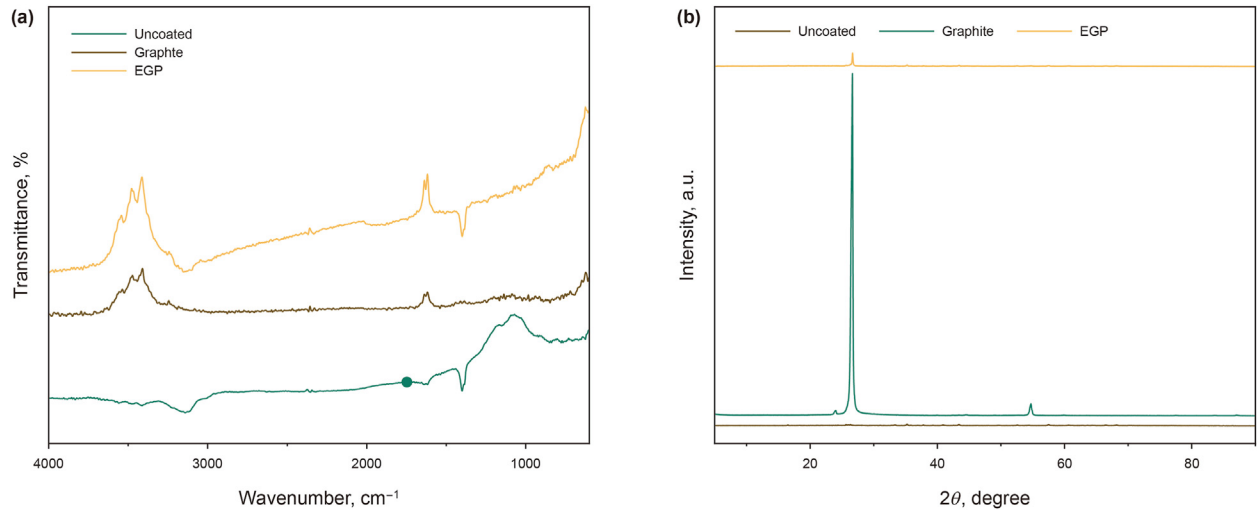

Fig. 4. (**a**) FT-IR spectra of the uncoated proppant (green), graphite (brown), and EGP (yellow). (**b**) XRD pattern of the uncoated proppant (green), graphite (brown), and EGP (yellow).

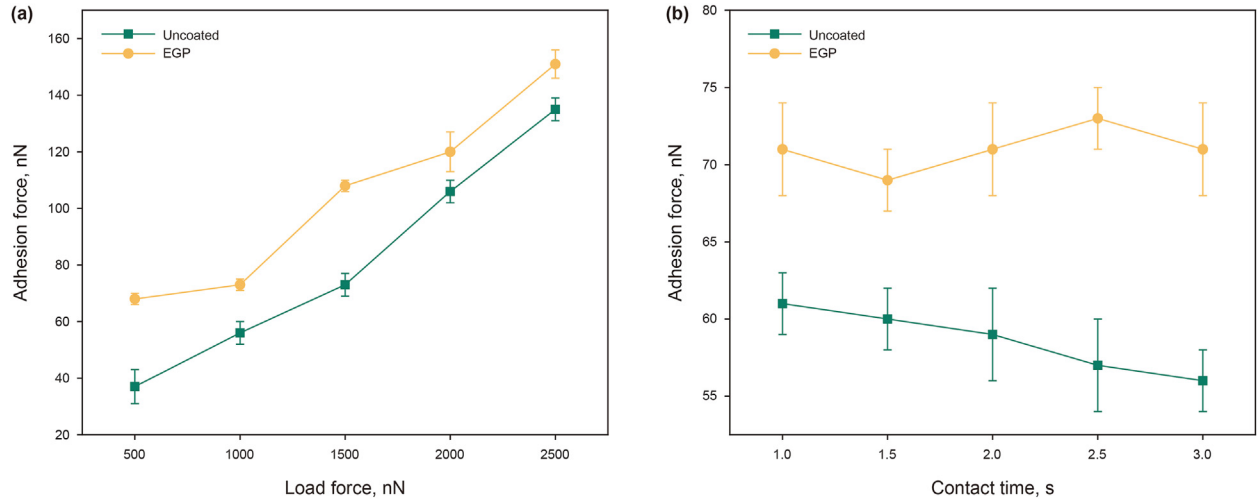

Fig. 5. Adhesion force of different proppants at different load forces (**a**) and contact time (**b**).

2.5. Suspending experiment

The guar gum solution was prepared in a fixed mass proportion (0.2 wt%). 2 g proppants were added to the guar gum solution and stirred at 450 r/min for 10 min. Part of the proppants was floated on the surface of the guar gum solution. Then the proppants floated on the solution were collected and weighed after drying.

2.6. Thermal conduction experiment

A glass petri dish containing proppant was placed on a heated table, while the temperature is 140 °C. The temperature of the proppant was tested by an infrared thermal imager (Testo 865). The heating device is a heating table (Wiggens wh220-ht).

3. Results and discussion

Fig. 2a displays the structure diagram of the EGP. Epoxy-resin was coated on the surface of commercial ceramic proppants, then graphite was coated on the epoxy-resin surface. Fig. 2b shows the SEM micrograph of the ceramic proppant, which indicates the surface of the ceramic proppant is rough. As shown in Fig. 2c, the surface of epoxy-resin coated proppant is smoother than the ceramic proppant. Fig. 2d is the SEM micrograph of the EGP, which barely affects the sphericity of the ceramic proppant. The graphite was coated on the proppant successfully from the SEM microscopes.

Fig. 3 shows the EDX results of different proppants. Aluminum element (Fig. 3c) and silicon element (Fig. 3d) were detected on the surface of the ceramic proppant. As for the epoxy-resin coated proppant, the sulfur element (Fig. 3j) can be observed, while aluminum element and silicon element were almost disappeared. Once the graphite was coated on the epoxy-resin coated proppant, the carbon element (Fig. 3l) on the surface of the EGP increased, while no other element. This confirms that the graphite was coated successfully on the surface of the proppant.

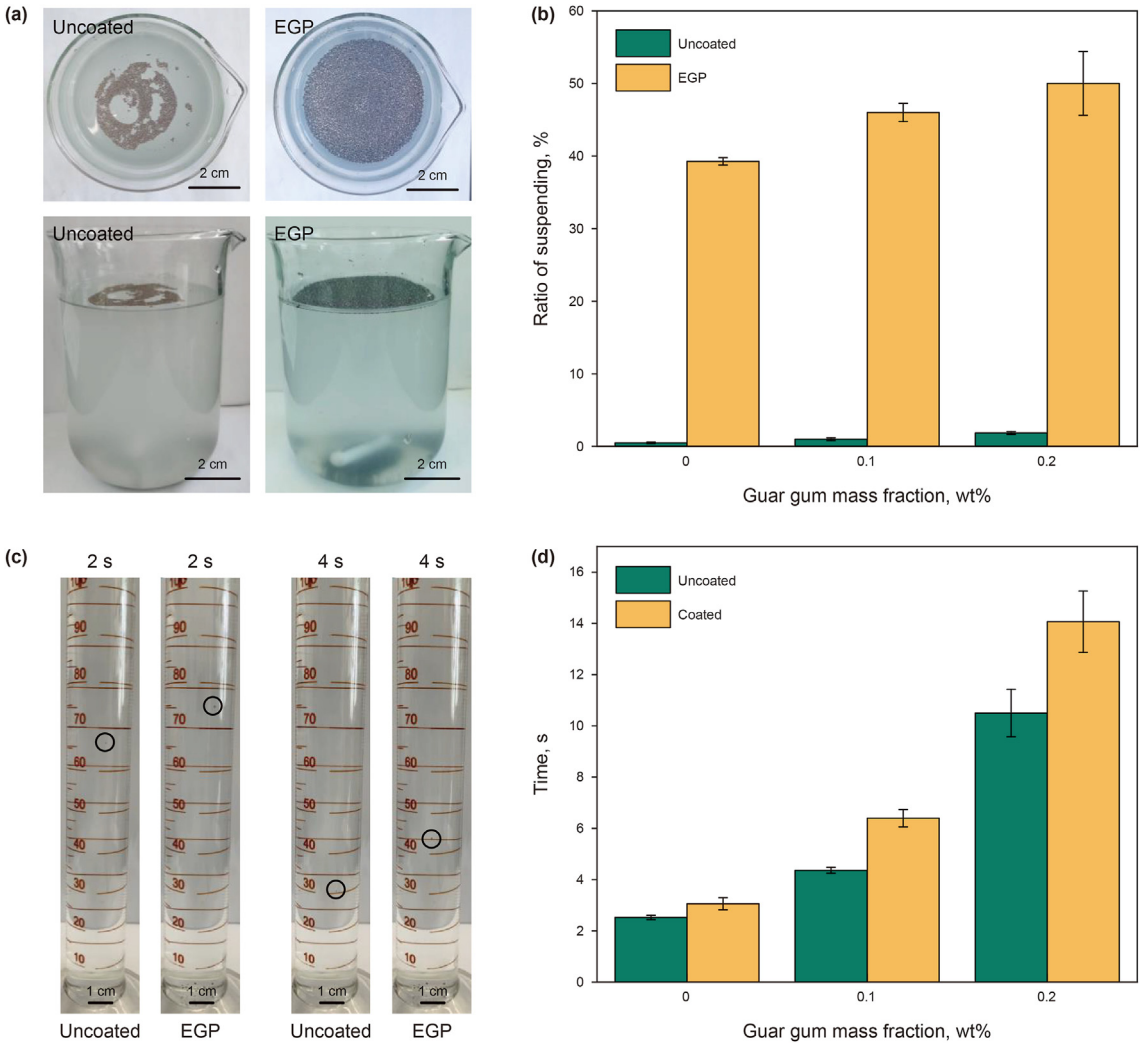

Fig. 6. (**a**) Images of suspending experiments of the uncoated proppants and EGPs. (**b**) Ratio of the suspending of different proppants at different guar gum mass fractions. (**c**) Falling images of different proppants in deionized water at different time points. (**d**) Falling time of different proppants at different guar gum mass fractions.

Fig. 4a represents the Fourier transform infrared (FT-IR) spectra of the three materials. For the graphite and the EGP characteristic peaks around 1618 and 3413 cm^{-1} were detected, which imply the presence of vibration of benzene ring and N—H. However, there was no similar characteristic peaks in the uncoated proppant. The change of characteristic peak proved the existence of graphite in proppant. Fig. 4b presents the results of the composition of the materials using XRD analysis, which indicates that the EGP has all the characteristic peaks of ceramic proppant and graphite. Moreover, a peak was detected at 26°, which is attributed to the graphite. This explained that the graphite adhered to the ceramic proppant successfully.

3.1. Adhesive properties

Fig. 5a shows the relationship between load force and adhesion force in different load force conditions. When the load force increased from 500 to 2500 nN, the adhesion force of uncoated proppant and EGP increased, which indicates that the graphite did not change the relationship between the adhesion force and the load force. Under the same load force, the adhesion force of the EGP is larger than the uncoated proppant, which is 45.6%, 23.3%, 32.4%, 11.7%, and 10.6% higher, respectively. The variation of adhesion forces between the EGP and the uncoated proppant in different contact time is shown in Fig. 5b. Once the contact time increases from 1 to 3.0 s and the load force was 1000 nN, the adhesion of the EGP remained at 71 nN, which shows that the adhesion of EGP and uncoated proppant did not change significantly with the increase of contact time. Moreover, when the load force is 1000 nN, the adhesion force of EGP is improved by 14.1%, 15.0%, 16.9%, 22.0%, and 21.1%, respectively. This indicates that the adhesion force of EGP is enhanced, which reduces the settlement of the proppant. Meanwhile, proppants are easier to adhere to the fracture crack, which will improve the effect of supporting fractures.

3.2. Suspending properties

Fig. 6a shows the suspending effect of the uncoated proppant and EGPs. Fig. 6b depicts that at the 0–0.2 wt% guar gum solution, the ratio of floating of EGPs is higher than that of the uncoated proppant, which is 77.5%, 45.0% and 26.0% higher, respectively. At different time points, the falling distance of EGPs in the guar gum

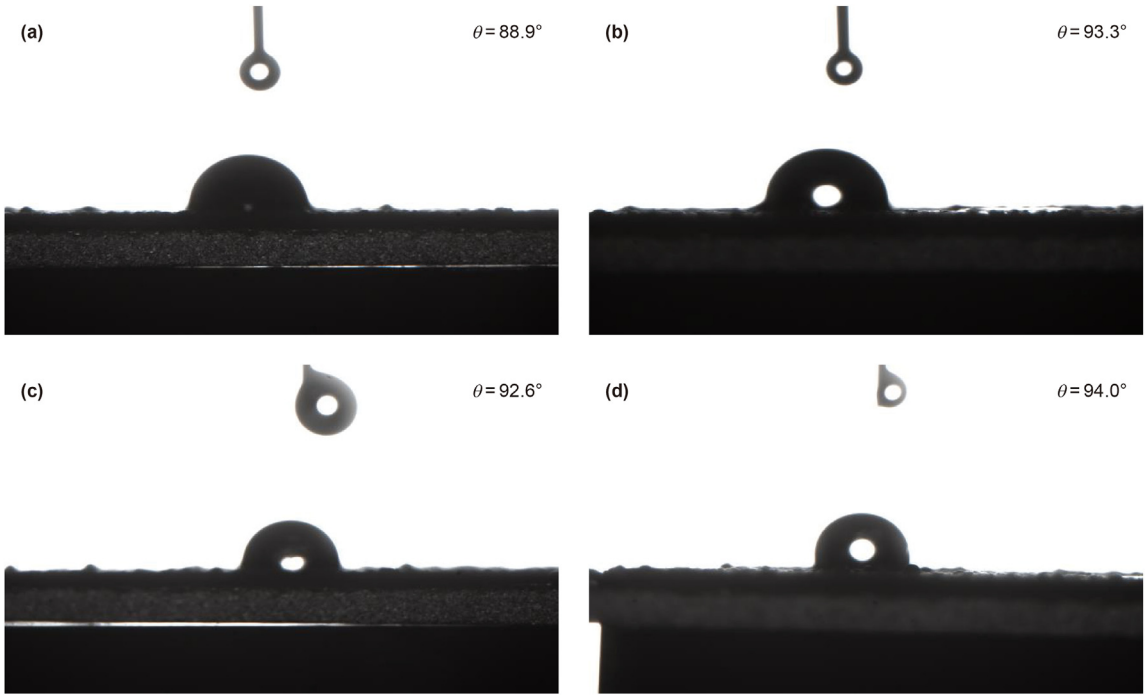

Fig. 7. Images of contact angle of uncoated proppants (**a, c**) and EGPs (**b, d**) in deionized water and the guar gum solution.

solution is smaller than that of the uncoated proppant (Fig. 6c). Fig. 6d shows the results of settling experiments, the falling time of the uncoated proppant and EGPs increases, which is due to the fact that the resistance of the solution increases with the increase in the guar gum mass fraction. At the same time, the falling time of EGPs is longer than that of the uncoated proppant, which is increased by 21.2%, 46.5%, and 34.0% higher, respectively. This indicates that the EGPs could move further into the deep fracturing crack.

3.3. Wettability

According to Fig. 7a and b, the contact angle of the uncoated proppants and EGPs is 88.9° and 93.3° in deionized water. At the same time, the contact angle of the uncoated proppant and EGPs is 92.6° and 94.0° in the guar gum solution (Fig. 7c and d). The contact angle of the EGPs increased by 4.9% and 1.5% in deionized water and the guar gum solution, respectively. The change of contact angle is negligible, which will not affect the flow rate of oil.

3.4. Thermal conduction properties and conductivity

Fig. 8a(i) shows the images of the uncoated proppants and EGPs before heating. Fig. 8b and c illustrates the results of the proppant thermal conductivity experiment at 140 °C, which illustrates that the temperature of the proppant increases with time. Fig. S1 in Supplementary Material displays the temperature variation of different materials, and the temperature of the materials increases with time. Meanwhile, the temperature of the EGPs is higher than that of the ceramic proppant at the same time point. The initial temperature of both uncoated proppants and EGPs is ~35 °C, after ~10 s, the temperature increasing speed of EGPs is 2.45 times that of uncoated proppants (Fig. 8a(ii)), while the largest contrast temperature is 84.6 °C at the 30 s. This indicates that the thermal conduction property of EGPs is better than the ceramic proppant. The EGPs transfer more heat than the ceramic proppant after the same time, which could provide more heat for the pyrolysis of the shale formation. As can be seen from Fig. 8d, the liquid conductivity of the uncoated proppants and EGPs decreases as the closure pressure increases from 5 to 45 MPa. However, the liquid conductivity of the EGPs is larger than that of the uncoated proppants, which is 21.4%, 10.3%, 4.7%, 6.2%, and 9% higher, respectively. This indicates that the oil and gas transportation efficiency could be improved by the EGPs.

4. Conclusions

The conversation of kerogen into oil and gas needs lots of heat in the exploitation of medium- and low-maturity shale oil. To transfer heat to the shale formation and support the fracturing crack, a novel proppant coated epoxy-resin e51 and graphite was prepared. To evaluate the properties of the novel proppant, numerous experiments were conducted such as adhesive experiment, suspending experiment, and thermal conduction experiment. The ratio of floating of EGPs is increased by 77.5% in deionized water. Besides, the liquid conductivity of EGPs is 21.4% higher than the uncoated proppant at the closure pressures of 5 MPa. The thermal conduction property of EGPs is enhanced by 245% compared with the uncoated proppant when the time point is 9 s. This indicates that the novel proppant with good suspending property and thermal conduction property is expected to be applied in the exploitation of shale oil.

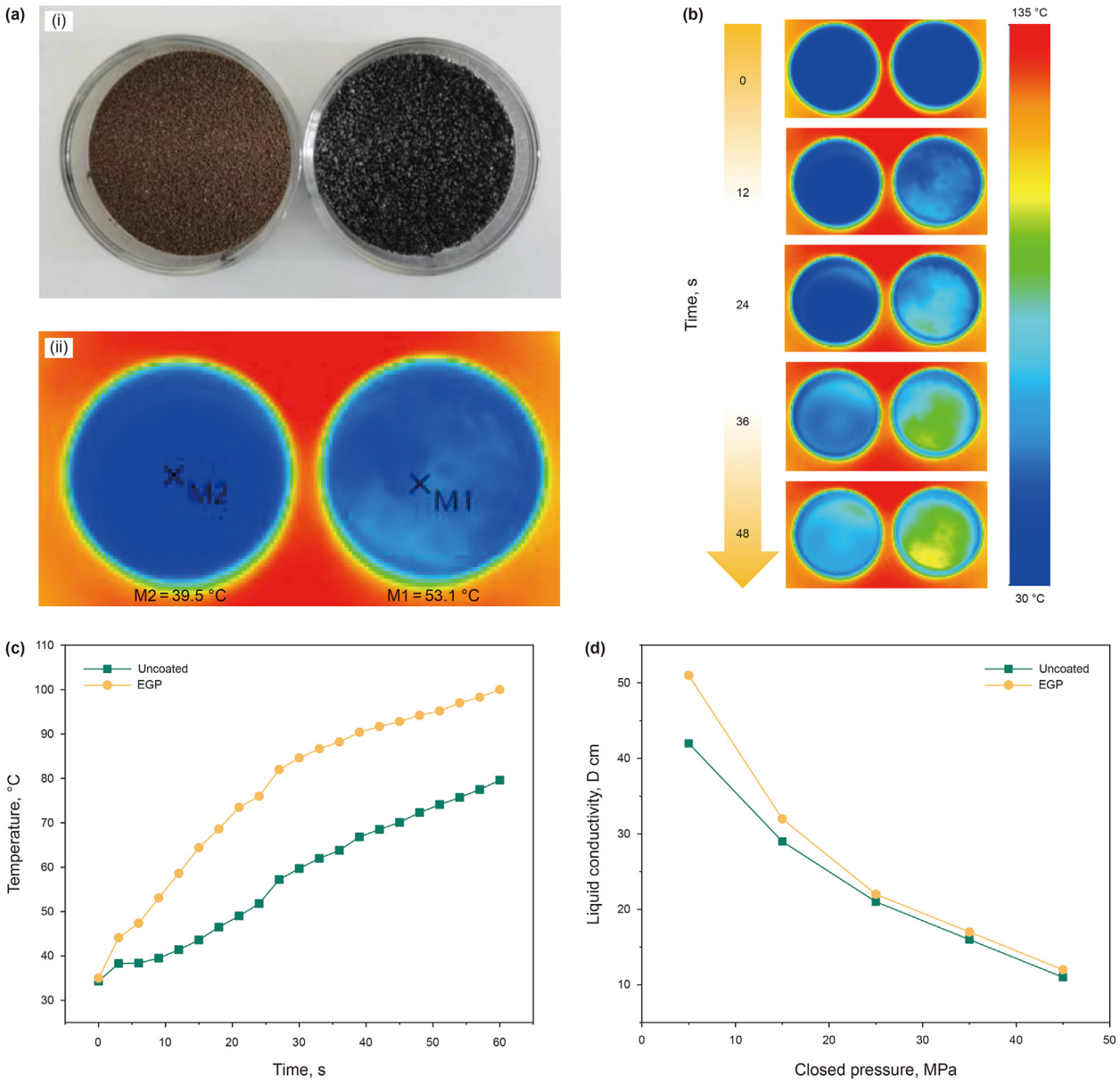

Fig. 8. (**a**) Images of the uncoated proppant and EGP before heating (i), and infrared thermal images of the uncoated proppant and EGP at a heating temperature of 140 °C (ii). (**b**) Infrared thermal images of the uncoated proppant and EGP at different time points. (**c**) Temperature of the uncoated proppant and EGP at different time points. (**d**) Liquid conductivity of the uncoated proppant and EGP at different closed pressures.

Acknowledgments

This work was supported by the National Key Research and Development Plan (No. 2020YFC1808102), General project of Beijing Natural Fund (No. 3222018), the Basic Research Program on Deep Petroleum Resource Accumulation and Key Engineering Technologies (No. U19B6003) and the Science Foundation of China University of Petroleum, Beijing (Nos. 2462020YXZZ018, 2462019BJRC007, 2462019BJRC007, 2462019QNXZ02).

Appendix A. Supplementary data

Supplementary data to this article can be found online at https://doi.org/10.1016/j.petsci.2022.11.022.

References

Bandara, K.M.A.S., Ranjith, P.G., Rathnaweera, T.D., et al., 2021. Crushing and embedment of proppant packs under cyclic loading: an insight to enhanced unconventional oil/gas recovery. Geosci. Front. 12 (6), 100970. https://doi.org/10.1016/j.gsf.2020.02.017.

Cao, W., Xie, K., Lu, X., et al., 2020. Self-suspending proppant manufacturing method

and its property evaluation. J. Petrol. Sci. Eng. 192, 107251. https://doi.org/10.1016/j.petrol.2020.107251.
Chen, M., Guo, T., Zou, Y., et al., 2021. Numerical simulation of proppant transport coupled with multi-planar-3D hydraulic fracture propagation for multi-cluster fracturing. Rock Mech. Rock Eng. 55 (2), 565–590. https://doi.org/10.1007/s00603-021-02694-7.
Danso, D.K., Negash, B.M., Ahmed, T.Y., et al., 2021. Recent advances in multifunctional proppant technology and increased well output with micro and nano proppants. J. Petrol. Sci. Eng. 196, 108026. https://doi.org/10.1016/j.petrol.2020.108026.
Faisal, H.M.N., Katti, K.S., Katti, D.R., 2020. Modeling the behavior of organic kerogen in the proximity of calcite mineral by molecular dynamics simulations. Energy Fuel. 34 (3), 2849–2860. https://pubs.acs.org/doi/10.1021/acs.energyfuels.9b03980.
Fu, L., Zhang, G., Ge, J., et al., 2016. Study on a new water-inhibiting and oil-increasing proppant for bottom-water-drive reservoirs. J. Petrol. Sci. Eng. 145, 290–297. https://doi.org/10.1016/j.petrol.2016.05.025.
Gai, H., Tian, H., Xiao, X., 2018. Late gas generation potential for different types of shale source rocks: implications from pyrolysis experiments. Int. J. Coal Geol. 193, 16–29. https://doi.org/10.1016/j.coal.2018.04.009.
Gol, R., Wang, C., Gupta, R.B., et al., 2017. Synthesis of self-suspending silica proppants using photoactive hydrogels. J. Petrol. Sci. Eng. 157, 651–656. https://doi.org/10.1016/j.petrol.2017.07.061.
Han, J., Sun, Y., Guo, W., et al., 2018. Non-isothermal thermogravimetric analysis of pyrolysis kinetics of four oil shales using Sestak–Berggren method. J. Therm. Anal. Calorim. 135 (4), 2287–2296. https://doi.org/10.1007/s10973-018-7392-7.
Han, X., Nie, J., Guo, J., et al., 2019. Rock physics modelling of elastic properties of organic shale considering kerogen stress and pore pressure distribution. J. Petrol. Sci. Eng. 174, 891–902. https://doi.org/10.1016/j.petrol.2018.11.063.
He, W., Sun, Y., Shan, X., 2021. Organic matter evolution in pyrolysis experiments of oil shale under high pressure: guidance for in situ conversion of oil shale in the Songliao Basin. J. Anal. Appl. Pyrol. 155, 105091. https://doi.org/10.1016/j.jaap.2021.105091.
Hu, S., Xiao, C., Liang, X., et al., 2019. The influence of oil shale in situ mining on groundwater environment: a water-rock interaction study. Chemosphere 228, 384–389. https://doi.org/10.1016/j.chemosphere.2019.04.142.
Hu, S., Bai, B., Tao, S., et al., 2022a. Heterogeneous geological conditions and differential enrichment of medium and high maturity continental shale oil in China. Petrol. Explor. Dev. 49 (2), 257–271. https://doi.org/10.1016/S1876-3804(22)60022-3.
Hu, S., Wu, H., Liang, X., et al., 2022b. A preliminary study on the eco-environmental geological issue of in-situ oil shale mining by a physical model. Chemosphere 287 (1), 131987. https://doi.org/10.1016/j.chemosphere.2021.131987.
Ju, Y., Zhu, Y., Zhou, H., et al., 2021. Microwave pyrolysis and its applications to the in situ recovery and conversion of oil from tar-rich coal: an overview on fundamentals, methods, and challenges. Energy Rep. 7, 523–536. https://doi.org/10.1016/j.egyr.2021.01.021.
Kang, Z., Zhao, Y., Yang, D., 2020. Review of oil shale in-situ conversion technology. Appl. Energy 269, 115121. https://doi.org/10.1016/j.apenergy.2020.115121.
Krishnan, M.R., Aldawsari, Y., Michael, F.M., et al., 2021. Mechanically reinforced polystyrene-polymethyl methacrylate copolymer-graphene and Epoxy-Graphene composites dual-coated sand proppants for hydraulic fracture operations. J. Petrol. Sci. Eng. 196, 107744. https://doi.org/10.1016/j.petrol.2020.107744.
Lan, W., Niu, Y., Sheng, M., Lu, Z., et al., 2020. Biomimicry surface-coated proppant with self-suspending and targeted adsorption ability. ACS Omega 5 (40), 25824–25831. https://doi.org/10.1021/acsomega.0c03138.
Lee, K.J., Finsterle, S., Moridis, G.J., 2018. Estimating the reaction parameters of oil shale pyrolysis and oil shale grade using temperature transient analysis and inverse modeling. J. Petrol. Sci. Eng. 165, 765–776. https://doi.org/10.1016/j.petrol.2018.03.020.
Li, H., Li, G., Yang, Q., et al., 2020. Modeling and performance analysis of shale oil and methane cogeneration by oil shale pyrolysis integrated with a pyrolysis gas methanation process. Energy Fuel. 34 (9), 11690–11698. https://doi.org/10.1021/acs.energyfuels.0c01709.
Li, J., Wu, M., Zhou, L., et al., 2022. A new proppant type fully coupled fiber-proppant and its property evaluation for unconventional reservoirs. J. Petrol. Sci. Eng. 208, 109573. https://doi.org/10.1016/j.petrol.2021.109573.
Luo, Z., Li, J., Zhao, L., et al., 2021. Preparation and characterization of a self-suspending ultra-low density proppant. RSC Adv. 11 (52), 33083–33092. https://doi.org/10.1039/D1RA05611E.
Meng, X., Bian, J., Li, J., et al., 2020. Porous aluminosilicates catalysts for low and medium matured shale oil in situ upgrading. Energy Sci. Eng. 8 (8), 2859–2867. https://doi.org/10.1002/ese3.704.
Pei, S., Wang, Y., Zhang, L., et al., 2018. An innovative nitrogen injection assisted in-situ conversion process for oil shale recovery: mechanism and reservoir simulation study. J. Petrol. Sci. Eng. 171, 507–515. https://doi.org/10.1016/j.petrol.2018.07.071.
Raja, M.A., Zhao, Y., Zhang, X., et al., 2017. Practices for modeling oil shale pyrolysis and kinetics. Rev. Chem. Eng. 34 (1), 21–42. https://doi.org/10.1515/revce-2016-0038.
Ren, X., Hu, Q., Liu, X., 2019. Nanoparticles patterned ceramsites showing super-hydrophobicity and low crushing rate: the promising proppant for gas and oil well fracturing. J. Nanosci. Nanotechnol. 19 (2), 905–911. https://doi.org/10.1166/jnn.2019.15730.
Sun, H., He, B., Xu, H., et al., 2022. Experimental investigation on the fracture conductivity behavior of quartz sand and ceramic mixed proppants. ACS Omega 7 (12), 10243–10254. https://doi.org/10.1021/acsomega.1c06828.
Taheri-Shakib, J., Kantzas, A., 2021. A comprehensive review of microwave application on the oil shale: prospects for shale oil production. Fuel 305, 121519. https://doi.org/10.1016/j.fuel.2021.121519.
Wang, H., Zhang, W., Qiu, S., et al., 2021. Release characteristics of Pb and BETX from in situ oil shale transformation on groundwater environment. Sci. Rep. 11 (1), 16166. https://doi.org/10.1038/s41598-021-95509-2.
Wang, L., Yang, D., Li, X., et al., 2018. Macro and meso characteristics of in-situ oil shale pyrolysis using superheated steam. Energies 11 (9). https://doi.org/10.3390/en11092297.
Wang, M., Guo, Z., Jiao, C., et al., 2019. Exploration progress and geochemical features of lacustrine shale oils in China. J. Petrol. Sci. Eng. 178, 975–986. https://doi.org/10.1016/j.petrol.2019.04.029.
Wang, Q., Hou, Y., Wu, W., et al., 2018. The structural characteristics of kerogens in oil shale with different density grades. Fuel 219, 151–158. https://doi.org/10.1016/j.fuel.2018.01.079.
Wang, S., Song, Z., Xia, J., et al., 2021. Quantitative determination of organic adsorption capacity in the Palaeozoic shales from South China. Energy Explor. Exploit. 39 (3), 779–796. https://doi.org/10.1177/0144598720983036.
Wang, Z., Lü, X., Li, Q., et al., 2020. Downhole electric heater with high heating efficiency for oil shale exploitation based on a double-shell structure. Energy 211, 118539. https://doi.org/10.1016/j.energy.2020.118539.
Xiao, H., Li, Z., He, S., et al., 2021. Experimental study on proppant diversion transportation and multi-size proppant distribution in complex fracture networks. J. Petrol. Sci. Eng. 196, 107800. https://doi.org/10.1016/j.petrol.2020.107800.
Xu, Q., Fan, F., Lu, Z., et al., 2021. Reversible adhesion surface coating proppant. Chin. Chem. Lett. 32 (1), 553–556. https://doi.org/10.1016/j.cclet.2020.02.014.
Xu, Y., Lun, Z., Pan, Z., et al., 2022. Occurrence space and state of shale oil: a review. J. Petrol. Sci. Eng. 211, 110138. https://doi.org/10.1016/j.petrol.2022.110183.
Yang, L., Liu, Z., Zeng, H., et al., 2021. Influence of gas flooding pressure on groundwater flow during oil shale in situ exploitation. Energies 14 (24). https://doi.org/10.3390/en14248363.
Yang, X., Zhang, L., Ye, T., et al., 2019. Research and economic analysis of the source-load coordination of oil shale exploitation. Math. Probl Eng., 4897156 https://doi.org/10.1155/2019/4897156.
You, Y., Han, X., Liu, J., et al., 2018. Structural characteristics and pyrolysis behaviors of Huadian oil shale kerogens using solid-state ^{13}C NMR, Py-GCMS and TG. J. Therm. Anal. Calorim. 131 (2), 1845–1855. https://doi.org/10.1007/s10973-017-6667-8.
You, Y., Han, X., Wang, X., et al., 2019. Evolution of gas and shale oil during oil shale kerogen pyrolysis based on structural characteristics. J. Anal. Appl. Pyrol. 138, 203–210. https://doi.org/10.1016/j.jaap.2018.12.025.
Zhang, C.P., Liu, S., Ma, Z.Y., et al., 2021. Combined micro-proppant and supercritical carbon dioxide (SC-CO_2) fracturing in shale gas reservoirs: a review. Fuel 305, 121431. https://doi.org/10.1016/j.fuel.2021.121431.
Zhang, Z., Guo, L., Zhang, H., et al., 2019a. Comparing product distribution and desulfurization during direct pyrolysis and hydropyrolysis of Longkou oil shale kerogen using reactive MD simulations. Int. J. Hydrogen Energy 44 (47), 25335–25346. https://doi.org/10.1016/j.ijhydene.2019.08.036.
Zhang, Z., Zhang, H., Chai, J., et al., 2019b. Reactive molecular dynamics simulation of oil shale combustion using the ReaxFF reactive force field. Energy Sources, Part A Recovery, Util. Environ. Eff. 43 (3), 349–360. https://doi.org/10.1080/15567036.2019.1624887.
Zhang, Z., Guo, L., Zhang, H., et al., 2020. A ReaxFF molecular dynamics study on the mechanism and the typical pyrolysis gases in the pyrolysis process of Longkou oil shale kerogen. Mol. Simulat. 46 (15), 1191–1199. https://www.tandfonline.com/doi/full/10.1080/08927022.2020.1809658.
Zhao, W., Hu, S., Hou, L., 2018. Connotation and strategic role of in-situ conversion processing of shale oil underground in the onshore China. Petrol. Explor. Dev. 45 (4), 563–572. https://doi.org/10.1016/S1876-3804(18)30063-6.
Zhao, W., Hu, S., Hou, L., et al., 2020. Types and resource potential of continental shale oil in China and its boundary with tight oil. Petrol. Explor. Dev. 47 (1), 1–11. https://doi.org/10.1016/S1876-3804(20)60001-5.
Zhu, J., Yang, Z., Li, X., et al., 2018. Application of microwave heating with iron oxide nanoparticles in the in-situ exploitation of oil shale. Energy Sci. Eng. 6 (5), 548–562. https://doi.org/10.1002/ese3.231.
Zoveidavianpoor, M., Gharibi, A., 2015. Application of polymers for coating of proppant in hydraulic fracturing of subterraneous formations: a comprehensive review. J. Nat. Gas Sci. Eng. 24, 197–209. https://doi.org/10.1016/j.jngse.2015.03.024.